CSIRO PUBLISHING

International Journal of Wildland Fire
http://dx.doi.org/10.1071/WF12040

Effects of distribution of bulk density and moisture content on shrub fires

Ambarish Dahale[A], *Selina Ferguson*[A], *Babak Shotorban*[A,B] *and Shankar Mahalingam*[A]

[A]Department of Mechanical and Aerospace Engineering, The University of Alabama in Huntsville, 5000 Technology Drive, Huntsville, AL 35805, USA. Email: ard0004@uah.edu; dovers@uah.edu; shankar.mahalingam@uah.edu
[B]Corresponding author. Email: babak.shotorban@uah.edu

Abstract. Formulation of a physics-based model, capable of predicting fire spread through a single elevated crown-like shrub, is described in detail. Predictions from the model, obtained by numerical solutions to governing equations of fluid dynamics, combustion, heat transfer and thermal degradation of solid fuel, are found to be in fairly good agreement with experimental results. In this study we utilise the physics-based model to explore the importance of two parameters – the spatial variation of solid fuel bulk density and the solid fuel moisture content – on the burning of an isolated shrub in quiescent atmosphere. The results suggest that vertical fire spread rate within an isolated shrub and the time to initiate ignition within the crown are two global parameters significantly affected when the spatial variation of the bulk density or the variation of fuel moisture content is taken into account. The amount of fuel burnt is another parameter affected by varying fuel moisture content, especially in the cases of fire propagating through solid fuel with moisture content exceeding 40%. The specific mechanisms responsible for the reduction in propagation speed in the presence of higher bulk densities and moisture content are identified.

Received 14 March 2012, accepted 13 November 2012, published online 25 March 2013

Introduction

The number of investigations using physics-based modelling to understand the behaviour of wildland fires has been lately increased. In physics-based modelling, both physical and chemical phenomena are taken into account to describe the fire behaviour (Sullivan 2009). Physics-based models, which seek numerical solutions to the governing physical equations, though much slower than real time, can be applied directly to a wide variety of scenarios. A review article recently published by Morvan (2011), discusses and compares the main features of four physics-based models including FIRESTAR, FIRETEC, WFDS and our model (Zhou *et al.* 2007; referred to therein as FIRELES). Several differences exist among these models, including: turbulence modelling approach, gas-phase combustion model, physical domain size, mesh size, etc. FIRESTAR uses an ensemble averaging approach to obtain the set of governing equations, which are then solved on a two-dimensional domain. On the other hand, in FIRETEC, WFDS and our model, the governing equations are based on large eddy simulation and the computational domain is three dimensional.

In this paper, we present a detailed formulation of our physics-based model applicable to the simulation of laboratory-scale fires. We use the model to study a configuration involving a 0.1 m-deep surface fuel bed, and elevated crown fuel situated 0.2 m above the surface fuel. The crown fuel represents a chamise (*Adenostoma fasciculatum*) shrub. Following the model formulation, we concentrate on two important physical parameters that influence fire spread rate to varying degrees: the spatial variation of the crown fuel bulk density and the fuel moisture content. We conduct the validation of the model through comparing its results against available experimental results. A laboratory-scale fire study, similar to our study, has been recently reported by Mell *et al.* (2009) who conducted experiments on the burning of a Douglas-fir (*Pseudotsuga menziesii*) tree to validate WFDS. Unlike in our study, the tree was modelled with a constant bulk density throughout the canopy volume and char oxidation was neglected. It is noted that some of the previous studies modelling large-scale fires have accounted for the non-uniform distribution of vegetation mass (see Grishin 1997 for details); however, studies conducted specifically on fire propagation through fuel beds describe a fuel matrix with a uniform distribution (Porterie *et al.* 2000; Morvan and Dupuy 2001; Zhou *et al.* 2005, 2007; Mell *et al.* 2007).

In this work we investigate the role of spatial variation of crown fuel bulk density, in determination of fire behaviour. The crown fuel bulk density refers to oven dry mass of foliage and small twig (less than 3 mm in diameter) per unit volume of canopy (Tachajapong 2008). Recent experimental measurements reveal that the bulk density of a chamise shrub, for instance, varies as a function of vertical height from its base and this variation is approximated with a cubic polynomial fit (Li 2011). The effect of two types of modelling of a solid fuel

matrix on fire spread rates is studied here. In one, no spatial variation for the bulk density within a shrub is considered (i.e. fixed bulk density (FBD)), whereas in the other the spatial variation of the bulk density is accounted for (i.e. a distributed bulk density (DBD) model is implemented).

The second focus of this work concerns the effect of fuel moisture on fire spread rates. From numerous field studies and experimental work (Anderson 1969; Pickford *et al.* 1980; Renkin and Despain 1992; Manzello *et al.* 2007), it is well known that solid fuel moisture content, formally defined as the mass of moisture per unit mass of dry solid fuel, influences fire spread phenomena considerably. Foliar moisture content is shown to be an important parameter in determination of quantity of heat required to initiate ignition in crown fuels (VanWagner 1977). Rothermel (1972) defined moisture of extinction as a threshold value of moisture content beyond which self-sustained combustion cannot occur inside the solid fuel matrix. Dimitrakopoulos and Papaioannou (2001) conducted flammability tests on various Mediterranean forest fuels under varying fuel moisture content and expressed the relationship between ignitability of the fuel and its moisture content with a linear regression fit. This model has been used to demonstrate that variation of time-to-ignition for different fuel samples can be explained through only one parameter: fuel moisture content. Babrauskas (2008) studied effects of fuel moisture content on burning of Douglas-fir trees, with important findings summarised as follows: samples with moisture content less than 30% were reported to burn completely with a rapid fire spread through the crown after ignition; samples with moisture content ranging from 30 to 70%, even though ignited successfully, were only partially consumed by the fire; and for samples with moisture content larger than 70%, only a small portion of crown mass was burnt beyond what is supported by the ignition mechanism.

In the next section, the methodology employed in the current study including various physical models adopted, is discussed in detail.

Mathematical models

Large eddy simulation (LES) is the method of choice to deal with turbulence in this study. In LES, given a generic field variable $f(\mathbf{x},t)$, which is a function of position vector $\mathbf{x}$ and time t, application of spatial filtering is expressed as:

$$\bar{f}(\mathbf{x},t) = \int f(\mathbf{x}',t)G(\mathbf{x},\mathbf{x}';\Delta)d\mathbf{x}' \tag{1}$$

where the overbar denotes a spatially filtered quantity. Here, G is a filter kernel function satisfying $\int G(\mathbf{x},\mathbf{x}';\Delta)d\mathbf{x}' = 1$, with Δ denoting the filter width, and the integration being performed over the spatial domain of interest. In this work a top-hat filter function in physical space is used to perform the filtering of transported quantities. The filter size is given by $\Delta = (\Delta V)^{1/3}$, where ΔV is the volume of the computational cell. For compressible flows, it is more convenient to work with density-weighted or Favre-filtered field quantities (Speziale *et al.* 1988), defined with a tilde as follows:

$$\tilde{f}(\mathbf{x},t) \equiv \overline{\rho f}/\bar{\rho} \tag{2}$$

The solid fuel matrix is modelled as a porous medium with gas phase porosity (ξ) and a packing ratio characterising the solid phase (β) (Larini *et al.* 1998). Because the solid phase contains multiple species (e.g. foliage and branches) we define $\beta = \sum_{L=1}^{n_L} \beta_L$, where β_L denote the fractional volumes occupied by the Lth solid species, and n_L is the total number of solid phase species. For a given typical control volume:

$$\xi + \sum_{L=1}^{n_L} \beta_L = 1 \tag{3}$$

ensures the conservation of volume and forms the basis of the multiphase formulation. The specific wetted area per unit volume (A_L) for the Lth solid phase is defined as $A_L = \beta_L \sigma_L$, where σ_L is the surface area to volume ratio for the Lth solid phase. In the case of cylindrical fuel elements, σ_L can be approximated via $\sigma_L = 4/d_L$ (Countryman and Philpot 1970), where d_L denotes the diameter of fuel particles from the Lth solid phase.

Gas-phase equations

The mathematical model for turbulent, compressible (low Mach number), reacting flows in the context of LES, includes the following set of governing equations:

$$\frac{\partial \bar{\rho}}{\partial t} + \frac{\partial \bar{\rho}\tilde{u}_i}{\partial x_i} = \sum_{L=1}^{n_L} \bar{S}_L \tag{4}$$

$$\frac{\partial \bar{\rho}\tilde{u}_i}{\partial t} + \frac{\partial \bar{\rho}\tilde{u}_i\tilde{u}_j}{\partial x_j} = \frac{\partial}{\partial x_j}\{-\bar{\rho}(\widetilde{u_i u_j} - \tilde{u}_i\tilde{u}_j)\} - \frac{\partial \bar{p}}{\partial x_i} + \frac{\partial \bar{\tau}_{ij}}{\partial x_j} + \bar{\rho}g_i - \sum_{L=1}^{n_L} \bar{F}_{L,i} \tag{5}$$

$$\frac{\partial \bar{\rho}\tilde{h}}{\partial t} + \frac{\partial \bar{\rho}\tilde{u}_j\tilde{h}}{\partial x_j} = \frac{\partial}{\partial x_j}\left\{-\bar{\rho}\left(\widetilde{u_j h} - \tilde{u}_j\tilde{h}\right)\right\} - \frac{\partial \bar{q}_i}{\partial x_i} + \frac{\partial \bar{q}_{\mathrm{rad},i}}{\partial x_i} - \sum_{L=1}^{n_L} \bar{q}_{\mathrm{conv},L} + \sum_{L=1}^{n_L} (1 - X_c)\dot{\bar{m}}_{\mathrm{char},L} E_L^{\mathrm{char}} + \sum_{L=1}^{n_L} \tilde{h} S_L \tag{6}$$

$$\frac{\partial \bar{\rho}\tilde{Y}_K}{\partial t} + \frac{\partial \bar{\rho}\tilde{u}_j\tilde{Y}_K}{\partial x_j} = \frac{\partial}{\partial x_j}\left\{-\bar{\rho}\left(\widetilde{u_j Y_K} - \tilde{u}_j\tilde{Y}_K\right)\right\} - \frac{\partial \bar{q}_{K,i}}{\partial x_i} + \sum_{L=1}^{n_L} \bar{S}_{L,K} + \bar{\omega}_K \tag{7}$$

$$\bar{p}_0 = \bar{\rho}\tilde{T}\mathrm{R}_u \sum_{K=1}^{n_K} \frac{\tilde{Y}_K}{W_K} \tag{8}$$

Here Eqns 4–7 are the respective filtered conservation equations for mass, ith component of momentum, energy and Kth gas phase species. Eqn 8 is the state equation for a multicomponent system of ideal gases, where $\bar{p}_0$ is the background pressure (Rehm and Baum 1978), which is assumed

constant and equal to one atmosphere, R_u is the universal gas constant, W_K denotes the molecular weight of the Kth gaseous species and n_K is the total number of gaseous species. In the above set of equations, $\bar{\rho}$ is the filtered gas mixture density, x_i is the component of the position vector in the ith direction, $\tilde{u}_i$ denotes the component of Favre-filtered velocity along x_i and t denotes time. In Eqn 4, the source term $\bar{S}_L$, is the filtered mass production rate resulting from decomposition of the Lth solid phase to gas phase. Term $\bar{S}_L$ is non-zero only within the solid fuel matrix.

In Eqn 5, $\bar{p}$ denotes the filtered first order pressure (Rehm and Baum 1978), g_i is the gravitational acceleration vector, $\bar{F}_{L,i}$ is the filtered ith component of the drag force resulting from the interaction between the gas and Lth solid phase; it is non-zero only within the fuel bed. A simple model for the drag force, of the form $\bar{F}_{L,i} = 0.5 C_{D,L} \bar{\rho} A_L |\tilde{\mathbf{u}}| \tilde{u}_i$, applicable to cylindrically shaped solid particles, is used. The drag coefficient $C_{D,L}$ for the Lth solid phase is approximated as proposed by Clift *et al.* (1978):

$$C_{D,L} = \frac{24\left(1 + 0.15\mathrm{Re}_{d_L}^{0.687}\right)}{\mathrm{Re}_{d_L}} \tag{9}$$

where, Re_{d_L} is the Reynold number defined in the 'Solid-phase equations' section.

The quantity $\bar{\tau}_{ij}$ in Eqn 5 represents the filtered viscous stress tensor, which is modelled using the standard Newtonian model based on filtered quantities:

$$\bar{\tau}_{ij} = -\frac{2}{3}\mu \frac{\partial \tilde{u}_k}{\partial x_k}\delta_{ij} + \mu\left(\frac{\partial \tilde{u}_i}{\partial x_j} + \frac{\partial \tilde{u}_j}{\partial x_i}\right) \tag{10}$$

Here μ is the dynamic viscosity of the gaseous mixture evaluated using a power law based on filtered temperature as in Bird (1994):

$$\mu = \mu_0 \left(\tilde{T}/T_0\right)^{0.6756} \tag{11}$$

where $\mu_0 = 1.983 \times 10^{-5}\,\mathrm{kg\,m^{-1}\,s^{-1}}$ and $T_0 = 300\,\mathrm{K}$.

In the filtered gas-phase energy equation (Eqn 6) $\tilde{h} = \sum_{K=1}^{n_K} \tilde{Y}_K \left(\Delta h^0_{f,K} + \int_{T_0}^{T} \bar{c}_{p,K}(\tilde{T}) d\tilde{T}\right)$ is the gas mixture enthalpy, $\Delta h^0_{f,K}$, $\bar{c}_{p,K}$ and $\tilde{T}$ are respectively the standard enthalpy of formation, heat capacity of the Kth gaseous species and the Favre-filtered gas temperature. n_K is total number of gaseous species. Curve-fit coefficients given in Kee *et al.* (1990) are used to calculate $\bar{c}_{p,K}$ values. The quantity $\bar{q}_i$ is the filtered heat flux vector modelled using the standard Fourier law based on filtered quantities as:

$$\bar{q}_i = -\frac{\mu}{\mathrm{Pr}} \tilde{c}_p \frac{\partial \tilde{T}}{\partial x_j} \tag{12}$$

where Pr (= 0.7) is the Prandtl number and $\tilde{c}_p(\tilde{T}) = \sum_{K=1}^{n_K} \tilde{Y}_K \int_{T_0}^{T} \bar{c}_{p,K}(\tilde{T}) d\tilde{T}$, is the specific heat of the gas mixture. The filtered source term $\bar{q}_{\mathrm{conv},L}$ denotes the convective heat transfer rate per unit volume between gas and the Lth solid phase, and $\bar{q}_{\mathrm{rad},i}$ is the radiative heat flux. The last two terms on the right-hand side (RHS) of Eqn 6 respectively describe the heat released from the heterogeneous combustion of char with oxygen and enthalpy associated with gases generated from thermal degradation of solid fuel. These terms are non-zero only within the solid fuel matrix. Here, $\bar{m}_{\mathrm{char},L}$ is the rate of char mass consumption per unit volume, E_L^{char} denotes the specific enthalpy associated with char combustion for the Lth phase and X_c (assumed to be 0.5 for all n_L solid phases (Baum and Street 1971)) is a fraction denoting the distribution of enthalpy of char combustion between the solid and gaseous phases.

In Eqn 7, $\tilde{Y}_K$ is the mass fraction of the gas-phase species K, $\bar{S}_{L,K}$ is the filtered production rate of the gas phase species K resulting from the decomposition of the Lth solid phase, and $\bar{\omega}_K$ is the filtered production rate of the gas-phase species K due to chemical reactions in the gas phase. In Eqn 7, $\bar{q}_{K,i}$ is the species diffusion flux modelled with the standard Fick's law:

$$\bar{q}_{K,i} = -\frac{\mu}{\mathrm{Sc}} \frac{\partial \tilde{Y}_K}{\partial x_j} \tag{13}$$

where Sc is the Schmidt number with a constant value of 0.7 for all species. Finally, the constraint $\sum_{K=1}^{n_K} \tilde{Y}_K = 1$ is imposed to solve for the mass fraction of the n_Kth species, often assumed to be gaseous nitrogen, N_2. The model for $\bar{\omega}_K$ is described in the 'Gas-phase combustion model' section.

The first terms on the RHS of Eqns 5–7 represent the unresolved scales of respective transported quantities, arising due to the filtering operation. In Eqn 5, $\sigma_{ij} \equiv \bar{\rho}\left(\widetilde{u_i u_j} - \tilde{u}_i \tilde{u}_j\right)$ is the subgrid-scale stress, calculated according to the Smagorinsky model (Yoshizawa 1986):

$$\sigma_{ij} = -2C_R \Delta^2 \bar{\rho} \sqrt{\Pi}\left(\tilde{S}_{ij} - \frac{1}{3}\tilde{S}_{kk}\delta_{ij}\right) + \frac{2}{3} C_I \Delta^2 \bar{\rho} \Pi \delta_{ij} \tag{14}$$

The second term on the RHS of Eqn 14 containing model constant C_I is neglected here due to its negligible contribution in low Mach number flows (Erlebacher *et al.* 1992). The resolved rate of strain tensor is:

$$\tilde{S}_{ij} = \frac{1}{2}\left(\frac{\partial \tilde{u}_i}{\partial x_j} + \frac{\partial \tilde{u}_j}{\partial x_i}\right) \tag{15}$$

where $\Pi = \tilde{S}_{ij}\tilde{S}_{ij}$ and subgrid eddy viscosity is:

$$\mu_t = C_R \Delta^2 \bar{\rho} \sqrt{\Pi} \tag{16}$$

Here, the model constant C_R is evaluated using a dynamic procedure proposed by Germano *et al.* (1991) with a modification made by Lilly (1991):

$$C_R = \frac{L_{ij}M_{ij} - \frac{1}{3}L_{kk}M_{ij}\delta_{ij}}{2M_{lm}M_{lm}} \tag{17}$$

where tensors M_{ij} and L_{ij} are functions of $\tilde{S}_{ij}$ and Π. The calculation of these functions involves another filtering operation called test filtering that uses a test filter of size $\hat{\Delta}$, larger than the grid size. In this work, the ratio of the test filter size to the

grid size is set to $\hat{\Delta}/\Delta = 2$ (Germano *et al.* 1991). A detailed procedure for the calculation of M_{ij} and L_{ij} can be found in Lilly (1991) with an extension made by Ghosal *et al.* (1995) to the statistically inhomogeneous flows. In Eqn 6, the subgrid scale energy flux is modelled as:

$$\bar{\rho}\left(u_j h - \tilde{u}_j \tilde{h}\right) = -\frac{\mu_t}{\mathrm{Pr}_t}\tilde{c}_p \frac{\partial \tilde{T}}{\partial x_j} \tag{18}$$

and in Eqn 7, the subgrid scale mass flux is modelled as:

$$\bar{\rho}\left(u_j Y_K - \tilde{u}_j \tilde{Y}_K\right) = -\frac{\mu_t}{\mathrm{Sc}_t}\frac{\partial \tilde{Y}_K}{\partial x_j} \tag{19}$$

where Pr_t and Sc_t are respectively subgrid scale Prandtl and Schmidt numbers; both are assumed to be equal to 0.7 (Branley and Jones 2001).

Solid-phase equations

For simplicity, the solid-phase fuel is considered stationary before, during and after the flame front has passed. The mass balance equation for the Lth solid phase is given by:

$$\frac{d\bar{m}_L}{dt} = -\dot{\bar{m}}_{L,\mathrm{H_2O}} - \dot{\bar{m}}_{L,\mathrm{pyr}} - \dot{\bar{m}}_{L,\mathrm{char}} \tag{20}$$

where $\bar{m}_L$ is the filtered mass per unit fuel bed volume of the Lth solid phase species, which in turn includes the filtered mass per unit fuel bed volume of water ($\bar{m}_{L,\mathrm{H_2O}}$), pyrolysis gases ($\bar{m}_{L,\mathrm{pyr}}$) and char ($\bar{m}_{L,\mathrm{char}}$). The corresponding filtered mass loss rate terms are denoted by $\dot{\bar{m}}_L$ with appropriate subscripts, and are deduced from Arrhenius-type laws. Because no data are currently available for burning of chaparral fuels, models proposed for pine needle combustion (Porterie *et al.* 2000) are used as follows:

$$\frac{d\bar{m}_{L,\mathrm{H_2O}}}{dt} = -\dot{\bar{m}}_{L,\mathrm{H_2O}} = -6.0\times10^5 \bar{T}_L^{-0.5} m_{L,\mathrm{H_2O}} \exp\left(\frac{-5800}{\bar{T}_L}\right) \tag{21}$$

$$\frac{d\bar{m}_{L,\mathrm{pyr}}}{dt} = -\dot{\bar{m}}_{L,\mathrm{pyr}} = -3.63\times10^4 m_{L,\mathrm{pyr}} \exp\left(\frac{-7250}{\bar{T}_L}\right) \tag{22}$$

$$\frac{d\bar{m}_{L,\mathrm{char}}}{dt} = -\dot{\bar{m}}_{L,\mathrm{char}} = -\frac{1}{r_1} 430\, A_L \rho_{\mathrm{O_2}} \exp\left(\frac{-9000}{\bar{T}_L}\right) \tag{23}$$

where r_1 is the oxygen to carbon stoichiometric mass ratio and $\rho_{\mathrm{O_2}}$ is the density of oxygen. The filtered production rate of Kth gaseous species, $\bar{S}_{L,K}$ (for water, and other gases released as a result of drying, pyrolysis and char combustion), present in Eqn 7 are given by:

$$\bar{S}_{L,\mathrm{H_2O}} = \dot{\bar{m}}_{L,\mathrm{H_2O}} \tag{24}$$

$$\bar{S}_{L,\mathrm{CO_2}} = \dot{\bar{m}}_{L,\mathrm{pyr}}\gamma_{\mathrm{CO_2}} + \dot{\bar{m}}_{L,\mathrm{char}} r_2 \tag{25}$$

$$\bar{S}_{L,\mathrm{O_2}} = \dot{\bar{m}}_{L,\mathrm{pyr}}\gamma_{\mathrm{O_2}} - \dot{\bar{m}}_{L,\mathrm{char}} r_3 \tag{26}$$

$$\bar{S}_{L,K} = \dot{\bar{m}}_{L,\mathrm{pyr}}\gamma_K \tag{27}$$

where γ_K is the fraction of the Kth gaseous species released via pyrolysis. The quantities r_2 and r_3 denote respectively the mass of gaseous CO_2 formed and O_2 consumed per unit mass of solid carbon burnt via char combustion, modelled using $C + O_2 \rightarrow CO_2$. Note that production of CO_2 and consumption of O_2 during char combustion is accounted for in Eqn 23. The filtered conversion rate of solid mass to gaseous mass $\bar{S}_L$, appearing in Eqn 4, is given by:

$$\bar{S}_L = \sum_{K=1}^{n_K} \bar{S}_{L,K} \tag{28}$$

The difference in σ_L for foliage and branches with different size is pronounced and hence it is reasonable to model the solid fuel matrix (shrub) as consisting of two phases: foliage (higher value of σ_L) and branches (lower value of σ_L). In the current work, 53% of the total solid mass per unit volume is that of foliage and 47% of the total solid mass is due to branches, as reported in Tachajapong (2008) for chamise shrubs. Surface area to volume ratio for foliage is taken to be $8000\,\mathrm{m^{-1}}$ and that for branches is $1800\,\mathrm{m^{-1}}$; physical density for foliage and branches are 500 and $600\,\mathrm{kg\,m^{-3}}$ (Countryman and Philpot 1970). At the subgrid scales, the solid fuel mass is assumed to have a uniform distribution. All n_L solid-phase species in a given fuel matrix are assumed to have the same moisture content.

Assuming that solid fuel particles are thermally thin (Atreya 1998), the energy balance equation for the Lth solid phase is:

$$\frac{d(\bar{c}_{p,L}\bar{m}_L\bar{T}_L)}{dt} = \bar{q}_{\mathrm{conv},L} + \bar{q}_{\mathrm{rad},L} + \bar{q}_{\mathrm{mass},L} \tag{29}$$

where $\bar{c}_{p,L} = 1.3\,\mathrm{kJ\,kg^{-1}\,K^{-1}}$ (Ragland *et al.* 1991) denotes the filtered specific heat of the Lth solid phase (assumed equal for all n_L phases) and $\bar{T}_L$ represents the filtered solid phase temperature. In Eqn 29:

$$\bar{q}_{\mathrm{conv},L} = A_L h_c (\tilde{T} - \bar{T}_L) \tag{30}$$

The heat transfer coefficient appearing in the above equation is deduced from the Nusselt number for the solid phase as $\mathrm{Nu}_L = h_c d_L/\lambda = 0.683\mathrm{Re}_{d_L}^{0.466}$, where λ is the gas-phase thermal conductivity, and the Reynolds number Re_{d_L}, is based on the diameter of the Lth fuel particle, the filtered gas-phase velocity and kinematic viscosity.

In Eqn 29, $\bar{q}_{\mathrm{mass},L}$, is modelled as:

$$\bar{q}_{\mathrm{mass},L} = -\dot{\bar{m}}_{L,\mathrm{H_2O}} E^{\mathrm{H_2O}} - \dot{\bar{m}}_{L,\mathrm{pyr}} E^{\mathrm{pyr}} + X_c \dot{\bar{m}}_{L,\mathrm{char}} E^{\mathrm{char}} \tag{31}$$

where E values with appropriate superscripts denote the associated enthalpies for the process of vaporisation, pyrolysis, and char combustion. The values used for these parameters in the present study are $E^{\mathrm{H_2O}} = 2250\,\mathrm{kJ\,kg^{-1}}$, $E^{\mathrm{pyr}} = 0.418\,\mathrm{kJ\,kg^{-1}}$ (Grishin 1997) and $E^{\mathrm{char}} = 32\,740\,\mathrm{kJ\,kg^{-1}}$ (Ragland *et al.* 1991). Here, $\bar{q}_{\mathrm{mass},L}$ represents the amount of heat exchanged between the gas and Lth solid phases.

The quantity $\bar{c}_{p,L}$ is deduced from the constant values for dry wood material and water (c_p^{dry}, $c_p^{\text{H}_2\text{O}}$), and the filtered mass fraction of moisture $\bar{Y}_L^{\text{H}_2\text{O}}$, in the Lth solid phase:

$$\bar{c}_{p,L} = \left(1 - \bar{Y}_L^{\text{H}_2\text{O}}\right)c_p^{\text{Dry}} + \bar{Y}_L^{\text{H}_2\text{O}}c_p^{\text{H}_2\text{O}} \tag{32}$$

The model for $\bar{q}_{\text{rad},L}$ in Eqn 29 is described in the following section.

Radiative heat transfer

The radiation transport equation (RTE) for an absorbing emitting, non-scattering two-phase media is written following Larini *et al.* (1998):

$$\mu_{i,j}\frac{\partial\tilde{\xi}\tilde{I}_i}{\partial x_j} = \xi a_g\left(\frac{\sigma\tilde{T}^4}{\pi} - \tilde{I}_i\right) + \sum_{L=1}^{n_L} a_L\left(\frac{\sigma\bar{T}_L^4}{\pi} - \tilde{I}_i\right) \tag{33}$$

where $\tilde{I}_i$ denotes the filtered radiation intensity per unit time per unit solid angle per unit area normal to the direction $\vec{\Omega}_i$ and $\mu_{i,j}$ denotes the direction cosines associated with this direction with respect to the Cartesian coordinate directions x_j. No summation is carried over index i. Here we have invoked the grey gas assumption, which is appropriate for fires from vegetative fuels (Mell *et al.* 2007). The total radiation intensity per unit time and unit normal area is then computed via:

$$G = \int_{4\pi} \tilde{I}_i d\Omega_i \tag{34}$$

Using G from this equation, the radiation heat source term in the energy equations for gas-phase and Lth solid phase, viz., Eqns 6 and 29 are computed as:

$$\frac{\partial\bar{q}_{\text{rad},i}}{\partial x_i} = \xi a_g(G - 4\sigma\tilde{T}^4) \tag{35}$$

$$\bar{q}_{\text{rad},L} = a_L(G - 4\sigma\bar{T}_L{}^4) \tag{36}$$

where a_g and a_L respectively denote the absorption coefficients for the gas and Lth solid phase and ξ is the gas-phase porosity as defined in Eqn 3. For propagation of a surface fire through pine needles or excelsior fuel beds, experimental measurements of the heat fluxes received by a radiometer have shown that the model, $a_L = \beta_L\sigma_L/4$ is appropriate (Butler 1993). In the case of a_g, we make the grey gas assumption and use the empirical model proposed by Kaplan *et al.* (1996), as follows:

$$a_g = 0.1(\bar{X}_{\text{CO}_2} + \bar{X}_{\text{H}_2\text{O}}) + 1862\tilde{f}_v\tilde{T} \tag{37}$$

in units of per metre, noting that temperature is in Kelvin. Though gas-phase species contribute negligibly to a_g as compared with soot, they are retained for the sake of generality. The soot phase absorptivity shown in the last term of Eqn 37 is that used in the RadCal package (Grosshandler 1993).

Soot particle transport and chemistry

Sophisticated models for soot particle evolution have been developed and used in the context of hydrocarbon–air turbulent jet flames (Wang *et al.* 2005; Mehta *et al.* 2010). Due to the lack of information on generation of soot from cellulosic fuels, we have retained a simple model in this work, which only accounts for evolution of soot volume fraction along with existing semi-empirical models, as described below. The soot volume fraction is evaluated via the model transport equation:

$$\frac{\partial\bar{\rho}\tilde{f}_v}{\partial t} + \frac{\partial\bar{\rho}(\tilde{u}_j + \tilde{u}_j^{\text{th}})\tilde{f}_v}{\partial x_j} = \frac{\partial}{\partial x_j}\left\{-\bar{\rho}\left(\widetilde{u_j f_v} - \tilde{u}_j\tilde{f}_v\right)\right\} - \frac{\partial\bar{q}_{f_v,i}}{\partial x_i} + \bar{\omega}_{f_v} \tag{38}$$

In the above equation, $\tilde{u}_j^{\text{th}}$ is the filtered thermophoretic velocity modelled by Kaplan *et al.* (1996) as:

$$\tilde{u}_j^{\text{th}} = -0.54\frac{\bar{\mu}}{\bar{\rho}}\frac{\partial\ln\tilde{T}}{\partial x_j} \tag{39}$$

where the instantaneous value of temperature is replaced by the filtered value (Dong and Chen 2011). The quantity $\bar{q}_{f_v,i}$ in Eqn 38 is the filtered soot diffusion flux vector, modelled using the standard Fick's law based on the filtered quantities as:

$$\bar{q}_{f_v,i} = -\frac{\mu}{\text{Sc}}\frac{\partial\tilde{f}_v}{\partial x_j} \tag{40}$$

and the subgrid scale flux of soot is modelled as:

$$\bar{\rho}\left(\widetilde{u_j f_v} - \tilde{u}_j\tilde{f}_v\right) = -\frac{\mu_t}{\text{Sc}_t}\frac{\partial\tilde{f}_v}{\partial x_j} \tag{41}$$

A semi-empirical model based on the work of Kaplan *et al.* (1996), for the source term $\bar{\omega}_{f_v}$ in which filtered quantities are used, is utilised. This model assumes that soot is formed primarily via pyrolysis of the solid fuel and neglects soot formation via combustion reactions occurring in the gaseous phase, and is given as:

$$\bar{\omega}_{f_v} = \frac{\bar{\rho}}{\rho_{\text{soot}}}\left(0.01\bar{m}_{s,\text{pyr}} - \frac{6\tilde{f}_v}{d_{\text{soot}}}W_{\text{NSC}}\right) \tag{42}$$

where ρ_{soot} denotes the density of solid soot particles, which is taken to be $1800\,\text{kg m}^{-3}$. A typical soot particle diameter value of $d_{\text{soot}} = 10\,\mu\text{m}$ is assumed. The sink term in Eqn 42 models soot oxidation via the Nagle and Strickland (NSC) oxidation mechanism, given by (Nagle and Strickland-Constable 1962):

$$W_{\text{NSC}} = 120\left[\frac{k_A P_{\text{O}_2}}{1 + k_z P_{\text{O}_2}}\chi + P_{\text{O}_2}(1 - \chi)\right] \tag{43}$$

where

$$\chi = \frac{1}{1 + \frac{k_T}{k_B P_{\text{O}_2}}} \tag{44}$$

Here, P_{O_2} is the partial pressure of oxygen and various reaction rates k_A ($kg\,m^{-2}\,s^{-1}\,atm^{-1}$), k_B ($kg\,m^{-2}\,s^{-1}\,atm^{-1}$), k_T ($kg\,m^{-2}\,s^{-1}$), k_z (atm^{-1}) occurring in the expression of W_{NSC} depend on the temperature in the following way (Nagle and Strickland-Constable 1962):

$$k_A = 200\,\exp(-30\,000/R\tilde{T}) \tag{45}$$

$$k_B = 4.46 \times 10^{-2}\exp(-15\,200/R\tilde{T}) \tag{46}$$

$$k_T = 1.51 \times 10^{6}\exp(-97\,000/R\tilde{T}) \tag{47}$$

$$k_z = 21.3\,\exp(4100/R\tilde{T}) \tag{48}$$

Gas-phase combustion model

The filtered chemical reaction rate terms appearing in the gas phase species transport equation (Eqn 7) are modelled using the flame surface density-based approach proposed by Zhou and Mahalingam (2002). Briefly, this filtered reaction rate is modelled as:

$$\bar{\omega}_K = \dot{M}_K\bar{\Sigma} \tag{49}$$

where $\dot{M}_K$ is the production or consumption rate of the Kth species per unit flame surface area per unit time (i.e. the flamelet consumption rate) and $\bar{\Sigma}$ denotes the available flame surface area per unit volume (i.e. the filtered flame surface density). The flamelet consumption rate is pre-computed for a steady, laminar, opposed flow diffusion flame of pyrolysis gas and air, for various strain rates using OPPDIF code (Kee *et al.* 1989) and stored in a lookup table which can be used while performing large eddy simulation. A one-step global reaction is described as follows:

$$\begin{aligned} &aCH_4 + bCO + cCO_2 + dH_2 + e(O_2 + 3.762N_2) \\ &\rightarrow\ (a+b+c)CO_2 + (2a+d)H_2O + e3.762N_2 \end{aligned} \tag{50}$$

where $e = 0.5(4a + b + d)$ is used as the gas-phase chemistry model (Zhou and Mahalingam 2003). Term $\bar{\Sigma}$ is modelled by $\bar{\Sigma}(x,t) = |\overline{\nabla Z(x,t)}|_{st}P_L(Z_{st};x,t)$, where Z is the mixture fraction (Zhou and Mahalingam 2003). Here, $|\overline{\nabla Z}|_{st}$ is the conditional filtered value of the mixture fraction gradient along the stoichiometric isosurface and $P_L(Z_{st};x,t)$ is the filtered probability density function of Z, defined according to its mean, its subgrid scale variance and assuming a β function distribution. Further description and details on modelling of these quantities can be found in Zhou *et al.* (2004).

Numerical methods and simulation setup

Fig. 1*b* shows the computational domain and the fuel setup. The dimensions of the computational domain are 1.6, 3.2 and 1.6 m in x, y and z directions. Our computations reveal that the results could be somewhat affected if the dimension of the domain in the vertical direction (y direction) is too short, e.g. 1.6 m. However, we have found that the results become insensitive to a change of the value of this dimension from 3.2 to 4.0 m. The rationale for the simulation setup (surface and crown fuel dimensions etc.) is guided by previous experimental conditions as discussed in the 'Results' section. The governing equations described in the 'Mathematical models' section are discretised in a three-dimensional Cartesian coordinate system on a uniform rectangular mesh, using finite-volume formulation and collocated variable arrangement.

For the gas-phase equations, the quadratic upwind interpolation for convective kinematics with estimated streaming terms (QUICKEST) finite volume scheme proposed by Leonard (1979), has been implemented. The QUICKEST scheme uses a quadratic upwind procedure for spatial discretisation of convective and diffusive terms of transport equations while using an explicit quadratic Leith-type of temporal discretisation method. Thus it maintains third-order accuracy in space and time. A detailed formulation of this scheme in multidimensional flows can be found in Pereira and Sousa (1993). Calculation of the time step is based on satisfying stability criteria dictated by Courant numbers, which are defined based on cell face convective velocities. To solve for pressure–density–velocity coupling, a fractional step method similar to that proposed by Kim and Moin (1985) is used, with the difference that our time integration procedure is fully explicit. Here, the momentum equations are solved at the first inner iteration without accounting for the pressure term. These momentum values are then projected on the continuity equation to obtain a Helmholtz equation for pressure (Mahesh *et al.* 2006). In every time step, several inner iterations are performed until density and momentum, at the new time step, satisfy the mass conservation equation within a specified error limit. The solid phase equations are time integrated using the forward Euler method.

The grid resolution used is $80 \times 160 \times 80$ in x, y, and z directions. The computations in the code are preformed through parallel processing, based on the MPI (message passing interface) protocol. All computations are done using 40 processors of a dense memory cluster (DMC, located at Alabama Supercomputing Center, Huntsville, AL) and 12 GB of memory. The CPU time and the wall time for 100 s of fire spread simulation respectively are ~5000 and 125 h. The LES model discussed above is based on an implicit filtering approach, in which changing the grid resolution causes the LES results to change. This change of results continues as the resolution increases until the results converge to the DNS (direct numerical simulation) results (Gullbrand and Chow 2003; Janicka and Sadiki 2005; Boudier *et al.* 2008). This means that LES converges to DNS when the grid size is in the order of the Kolmogorov length scale. Also, in chemically reacting flows, additional complications exist. For example, chemical reaction zones are smaller than the smallest turbulence length scales and resolving them completely is computationally demanding. Because of this, the grid resolution study is not relevant to the LES modelling based on the implicit filtering. Our approach in selecting this grid resolution was guided by the extensive grid independence study carried out in a closely related work (Zhou *et al.* 2005; governing equations based on Unsteady-RANS and two-dimensional computations); where the solid phase combustion model, thermal radiation

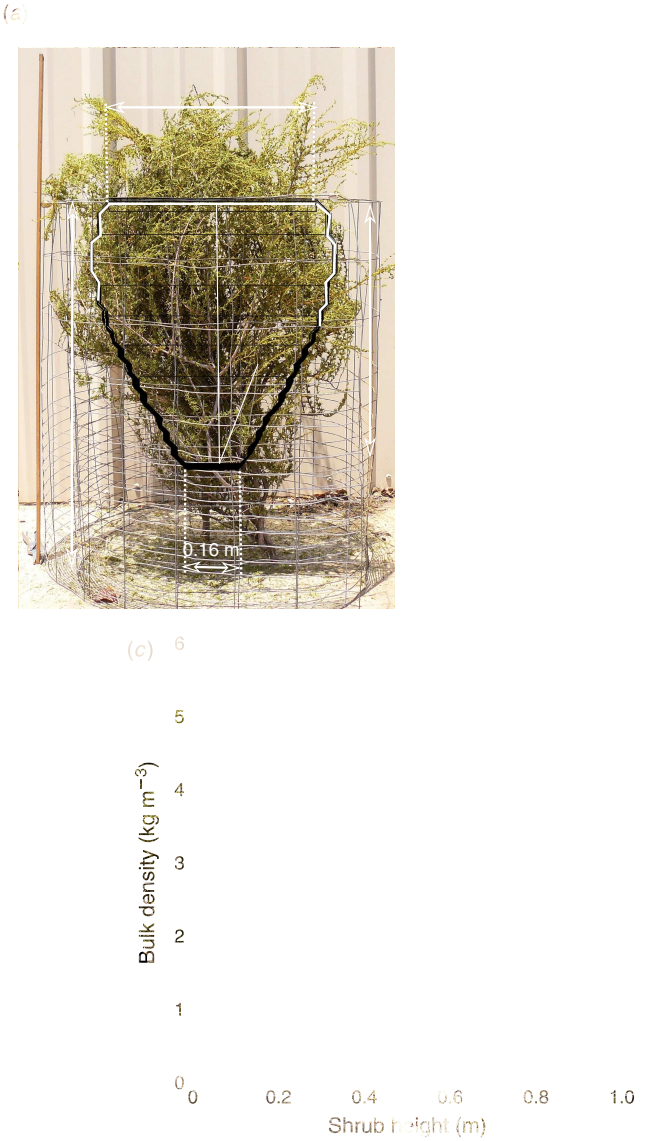

Fig. 1. (*a*) Computational shrub superimposed on the image of a real chamise shrub; (*b*) 3-D view of the modelling setup; (*c*) Bulk density distribution for chamise as a function of shrub height (Li 2011).

model and the computational parameters involved are exactly the same as those used by us. Later Zhou *et al.* (2007), using the same LES model and grid resolution (discussed above), showed a good comparison between computational and experimental results. Therefore the grid resolution chosen represents a balance in obtaining results that are considered nearly independent of computational parameters.

The entire computational domain is initialised with zero velocities. Open boundary conditions, wherein gradients normal to boundary are set to zero, are implemented for all except the bottom boundary. A closed boundary condition is used for the bottom, i.e. no inflow or outflow can take place through this boundary.

The discrete ordinates method (DOM) proposed by Chandrasekhar (1960) is used to compute intensities in n discrete directions per octant. The value of n is given by $N(N+2)$ where N is the index of S_N-method used. This method transforms the RTE, i.e. Eqn 33, into n simultaneous partial differential equations where each equation represents one discrete direction. Theoretical details and solution techniques can be found in Modest (2003). The integral appearing in Eqn 34 is evaluated using a rectangular quadrature approximation as given by:

$$G = \sum_{i=1}^{n} w_i I_i \tag{51}$$

where w_i is the discrete solid angle in the ith direction over which radiative intensity is considered to be constant. In this work S_6 approximation of the S_N discrete ordinates method is used, which

Table 1. Crown fuel bulk density and solid fuel moisture content in various cases
In all cases, the shape of the shrub is the same

Case number	Crown fuel bulk density model	Solid fuel moisture content
1	Distributed	31.2%
2	Fixed	31.2%
3a to 3e	Distributed	[A]
4a to 4e	Fixed	[A]

[A]Subcases: a, b, c, d and e are for 20, 40, 60, 80 and 100% moisture content.

Table 2. Initial conditions of crown fuel during experiment and simulation of Case 1 (see Table 1)

Average bulk density of crown fuel	3.8 kg m^{-3}
Total height of crown fuel	1.0 m
Sample diameter (crown fuel largest diameter)	0.7 m
Bottom surface diameter (crown fuel)	0.16 m
Top surface diameter (crown fuel)	0.56 m
Total initial mass of crown fuel	0.7 kg
Crown fuel moisture content	31.2%

requires evaluation of radiative intensities in $n = 48$ directions. The weights associated with the quadrature approximation in Eqns 51 and direction cosines used in Eqns 33 are those provided by Lathrop and Carlson (1965) and reproduced in Modest (2003).

Results

While calculating bulk density of the fuel matrix, the mass of all n_L solid phase species is taken into account. In all the results to be presented, the surface fuel (aspen excelsior) has dimensions of 0.8, 0.1 and 0.8 m in $\boldsymbol{x}$, $\boldsymbol{y}$, and $\boldsymbol{z}$ directions, and is modelled as a single solid-phase species with a constant bulk density of 3.125 kg m^{-3}. Total wet mass of surface fuel is 250 g, similar to that used in experiments. The shape of the crown-like elevated fuel is modelled as a conical frustum with its diameter changing as a function of its height. As a first approximation, the functional dependence of crown diameter on height ($\boldsymbol{y}$) is modelled using a cubic polynomial. Fig. 1*a* shows an image of a typical chamise shrub, on which a computational shrub image has been superimposed. For the crown fuel that we study $n_L = 2$, as the shrub contains branches and foliage. All simulations are performed under no wind, zero slope conditions. The conditions used for simulation of various cases are summarised in Table 1. Solid fuel parameters to be presented are mass averaged over n_L solid phase species.

In the experimental work of Li (2011), which is used for the validation of modelling results, the ignition of the surface fuel is carried out by spraying 10 mL of isopropyl alcohol in the ignition region and then supplying external heat to this region (using a torch flame). Isopropyl alcohol is used to establish uniform burning of fuel in the ignition region. In computations, the temperature of solid fuel in the ignition zone is raised and maintained to 1000 K by supplying external heat to achieve ignition and uniform burning. The external heat source is turned off when 80% of fuel in the ignition zone is consumed. Because surface fuel in all of the simulations performed was kept the same, the igniter gets turned off after ~7 s. In the experiments, Li (2011) observed the time history of gas-phase and solid-phase temperatures, at the centre of the ignition zone, to match that obtained from computations; hence, we adopt the same ignition mechanism. The dimensions of the ignition zone ($0.15 \times 0.1 \times 0.15$ m in $\boldsymbol{x}$, $\boldsymbol{y}$ and $\boldsymbol{z}$ directions) used in experiments are kept the same while performing computations.

Model validation

The various sub models described in the 'Mathematical models' section, combined with the computational methodology summarised in the 'Numerical methods and simulation setup' section, for the simulation of fire spread through live shrubs, are used to conduct a systematic analysis on the importance of various parameters necessary to describe fire behaviour. In order to do so, it is first necessary to test model predictions against experimental results. Here we use the experimental results obtained by Li (2011) for validation purposes. Because a DBD model better represents a realistic shrub as utilised in the experiments, Case 1 is selected for validation purposes over Case 2 (refer Table 1 for case description), which uses a FBD model. The performance of DBD and FBD models will be compared later in the 'Effect of distribution of bulk density' section.

The experiments (Li 2011) were performed in an open wind tunnel at the University of California–Riverside. Chamise was used as the crown fuel with a medium bulk density (bulk density ranging from 3.17 to 4.2 kg m^{-3} considered medium), zero wind speed and a centre ignition. Additional details on experimental setup, data acquisition and post processing can be found in Li (2011). The geometry and physical properties of the modelled crown, such as the total height, initial mass, bulk density, moisture content, etc., are set to match the properties of the actual chamise shrub, in a global sense (Table 2). It is noted that there still exist local heterogeneities in the actual shrub that are neglected in the model shrub. Therefore, only the global features of fire behaviour in experiments and simulations are compared against each other.

In Case 1 and Cases 3a–e of Table 1, the bulk density of the crown fuel is spatially distributed along the vertical direction, with distribution modelled as a polynomial function of vertical space variable given as follows:

$$\rho_B = A + B\hat{y} + C\hat{y}^2 + D\hat{y}^3 \qquad (52)$$

where $\hat{y} = y/H$, with y and H as the vertical spatial variable and the height of the shrub. This polynomial, as shown in Fig. 1*c*, has been recently proposed and is based on experimental measurements with $A = -0.025$, $B = 32.325$, $C = -58.746$ and $D = 29.239$ for chamise (Li 2011).

The overall time evolution of the fire, i.e. the ignition at the surface fuel and the transition from the surface to crown fuel, can be seen in Fig. 2, in which the contour plots of the gas-phase temperature (colour contours) and the solid fuel bulk density (line contours) are displayed on an $\boldsymbol{xy}$-slice passing through the domain at $\boldsymbol{z} = 0.8$ m, at various instants of time. It is observed that a low intensity flame is established in the ignition zone at

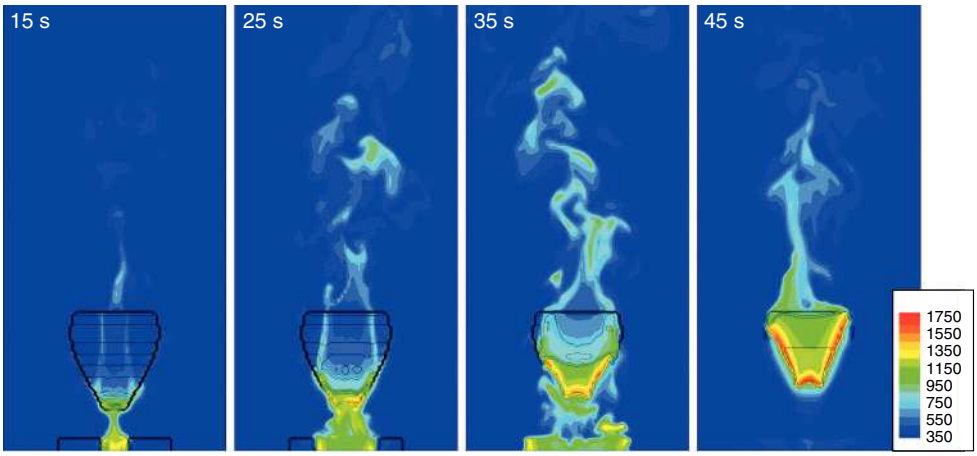

Fig. 2. Gas-phase temperature (K) (colour contours) with solid fuel bulk density (line contours) at various times for Case 1 (see Table 1). Snapshots are from a ***xy***-slice passing through $z = 0.8$ m.

earlier times during simulation when the igniter is on. The surface fuel is ignited at the centre below the base of crown fuel. This type of ignition represents a basic example of a spotting fire, commonly seen during wildland fires. As more mass in the ignition zone begins to burn, the intensity of the fire increases, which enhances the amount of heat transferred to neighbouring fuel elements. Because the igniter gets turned off at fairly early times (7 s) in the simulation, the effect of the igniter on computational results can be considered negligible.

Fig. 3 shows the relative importance of the convection and radiation heat transfer in igniting fuel particles at two different locations. Point 1 is located at the base of the crown fuel and point 2 is on the surface fuel just outside the ignition zone. In the initial stages of burning, fuel particles located at the base of the crown fuel receive more heat through convection compared with that received in the form of thermal radiation. In contrast, for fuel particles located on the surface fuel outside the ignition zone radiation plays a major role in starting the burning process. This difference in the heat transfer mechanism at two locations is due to the flow field resulting from the buoyancy effects. Cold air entering the ignition zone from outside leads to convective cooling of fuel particles at point 2, whereas the hot combustion gases (which tend to rise up from flames) heat the crown fuel base in a convective sense, including where point 1 is located. Ignition occurs in the crown fuel at ~8.4 s when the temperature of solid fuel at point 1 reaches 500 K, when pyrolysis and char oxidation processes commence. Crown fire initiation time, calculated based on solid fuel temperature averaged over the ***xz***-surface located at $y = 0.3$ m, for this case is 10.8 s. The burn is completed when the mass loss rate, $m = -dm/dt$, for the crown fuel equals zero. The burn time for Case 1 is ~82 s.

Table 3 shows a comparison between experimentally obtained data and numerical simulation predictions. Parameters such as burning time, total mass consumed, spread rates and the time required to reach maximum mass loss rate are in good agreement. The spread rate calculation from simulation data is based on average solid phase temperature, and is representative of an average rate of vertical spread. As the flow field generated is three dimensional and does not have homogeneity in any direction, averaging of the solid phase temperature is performed

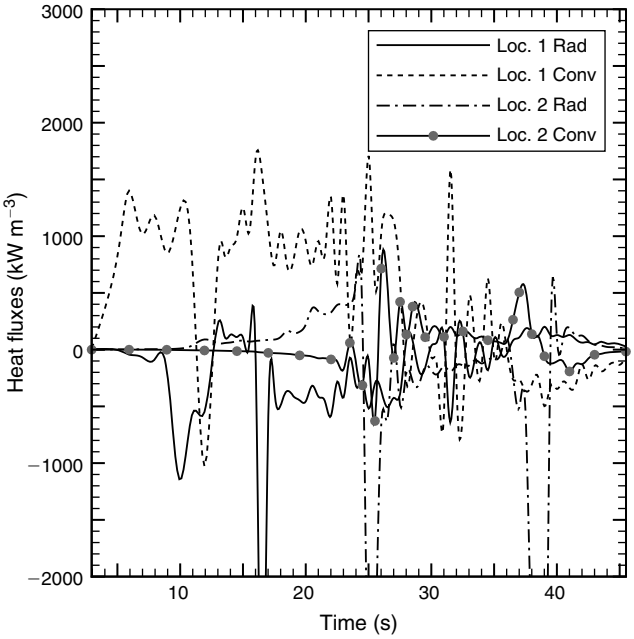

Fig. 3. Time history of radiation and convection heat fluxes ($\bar{q}_{\mathrm{rad},L}$ and $\bar{q}_{\mathrm{conv},L}$ from Eqn 29) at two spatial locations for Case1 (see Table 1). Location 1: $x = 0.8$ m, $y = 0.3$ m, $z = 0.8$ m (a point on the base of crown fuel). Location 2: $x = 1.0$ m, $y = 0.05$ m, $z = 0.8$ m (a point on surface fuel outside ignition zone). Positive heat flux means heat is transferred from gas phase to solid fuel particle and negative heat flux means vice versa.

on horizontal surfaces (***xz***-plane) at various ***y*** locations along crown fuel height. Vertical spread rate is calculated as follows:

$$\mathrm{ROS}_y = \frac{\sum_{i=1}^{M} \left(\frac{y_{i+1} - y_i}{t_{500,i+1} - t_{500,i}} \right)}{M - 1} \tag{53}$$

here ROS_y is the average spread rate in a ***y*** direction, y_i is the location of the *i*th horizontal ***xz*** surface of crown fuel along the ***y*** axis, $t_{500,i}$ is the time required by solid fuel in this horizontal

Table 3. Parameters concerned with global behaviour of fire in experiments and simulations

Two values seen for experiments are based on two repetitions of the experiments (Li 2011) with respective crown fuel bulk densities of $\rho_B = 3.17$ and 4.42 kg m^{-3}. Computational results are for Case 1 (see Table 1)

Results	Experimental	Computational
Fire spread rate along y, in crown fuel (mm s^{-1})	25.3; 23.2	27.0
Fire spread rate along x, in surface fuel (mm s^{-1})	5.88; 6.21	4.0
Maximum mass loss rate (g s^{-1})	30.0; 31.0	44.0
Time required to reach maximum mass loss rate (s)	32; 45	34
Burning time (s)	73; 112	82
Mass consumed, crown fuel (g)	402; 553	493

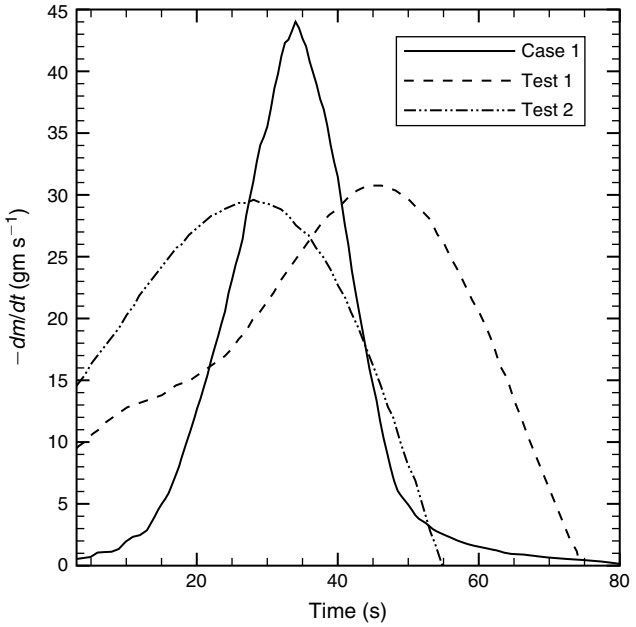

Fig. 4. Time history of mass loss rate from experiments (Test 1 and Test 2) conducted by Li (2011) and from simulation of Case 1 (from Table 1).

surface to reach the average temperature equivalent to 500 K and M is the total number of surfaces considered for spread rate calculation. For all simulations M is set equal to 8, i.e. the horizontal surfaces separated by a distance of 0.1 m are used for averaging. The horizontal fire spread rate in surface fuel was measured by observing the solid-phase temperature contour of 500 K, along an $\boldsymbol{xz}$-slice passing through $\boldsymbol{y} = 0.05$ m at various times.

The time history of mass loss rate obtained from computation matches well with experiments in a global sense, which can be seen from Fig. 4, but the predicted value of maximum mass loss rate differs considerably from experimental results (overestimated by a factor of 1.4). This difference may be attributed to the following reason: the crown fuel model accounts for the distribution of mass only in the vertical direction whereas in a real shrub, mass is non-uniformly distributed in all three directions. Distribution of mass also varies from shrub to shrub of the same species. Because the functional form of mass distribution in directions other than $\boldsymbol{y}$ is unknown, bulk density is kept constant along these directions in the current crown fuel model. Another source of error leading to discrepancies between computational and experimental results is the uncertainty involved in the experimental measurements. For example, FFT (fast Fourier transform)-based smoothing was applied to the time history of mass that was obtained from experiments, before calculating the mass loss rate. This procedure, although necessary for removing high frequency white noise from the data, may also lower the peak values.

Next, we highlight the importance of two physical parameters involved in the current fire propagation problem with the aid of the simulation results.

Effect of distribution of bulk density

In this section we compare the performance of two models used to represent the bulk density of the crown fuel. In the first model (Case 1 in Table 1), the bulk density of the shrub is spatially distributed along the vertical axis as described by Eqn 52 and shown in Fig. 1*c*. In the second model, used in the simulation of Case 2 from Table 1, the bulk density is kept constant, equal to 3.87 kg m^{-3}, throughout the crown fuel volume. The fixed bulk density value represents the average of the polynomial distribution given by Eqn 52. The simulation setup, geometric and the other physical properties of the solid fuel, boundary and initial conditions are kept the same in simulations of Case 1 and Case 2.

Fig. 5 shows the time evolution of the gas-phase and solid-phase temperatures averaged on the bottom and top surfaces of the crown fuel. Averaging is performed along the $\boldsymbol{xz}$-planes as the bulk density remains constant in this plane for both cases. As it can be seen in this figure, the time history of the bottom surface temperature (gas and solid phase) for Case 1 is not significantly different from that in Case 2. On the other hand, the time history of temperature (gas and solid phase) for the top surface of crown fuel obtained from Case 1 is considerably different from that for Case 2. This difference indicates that fire propagation rate inside the crown fuel matrix changes when bulk density distribution is accounted for. For both cases, the crown fire initiation time is $t = \sim 11$ s, i.e. when the average solid phase temperature at the bottom surface of the crown fuel reaches 500 K. In Fig. 6*a*, t_{500} is the time (s) required by a horizontal surface in the crown fuel to reach a temperature equal to 500 K, which is plotted as a function of shrub height. Fig. 6*b* shows the spread rate (mm s^{-1}) as a function of the height of the crown fuel. The fire spread rate in the lower part of the crown for the DBD case is observed to be lower than that in the FBD case whereas in the upper region fire spreads relatively faster for DBD than for FBD. This difference in spread rates for these two models can be explained based on bulk density values encountered for different regions while moving along the vertical axis. The lower half of the crown with DBD has a higher bulk density compared with crown with FBD, which creates a higher resistance for the hot combustion gases to penetrate into the crown fuel matrix, resulting in lower spread rates. Fig. 7 shows the total energy, viz., $\bar{q}_{\text{conv}} + \bar{q}_{\text{rad}} + \bar{q}_{\text{mass}}$ in

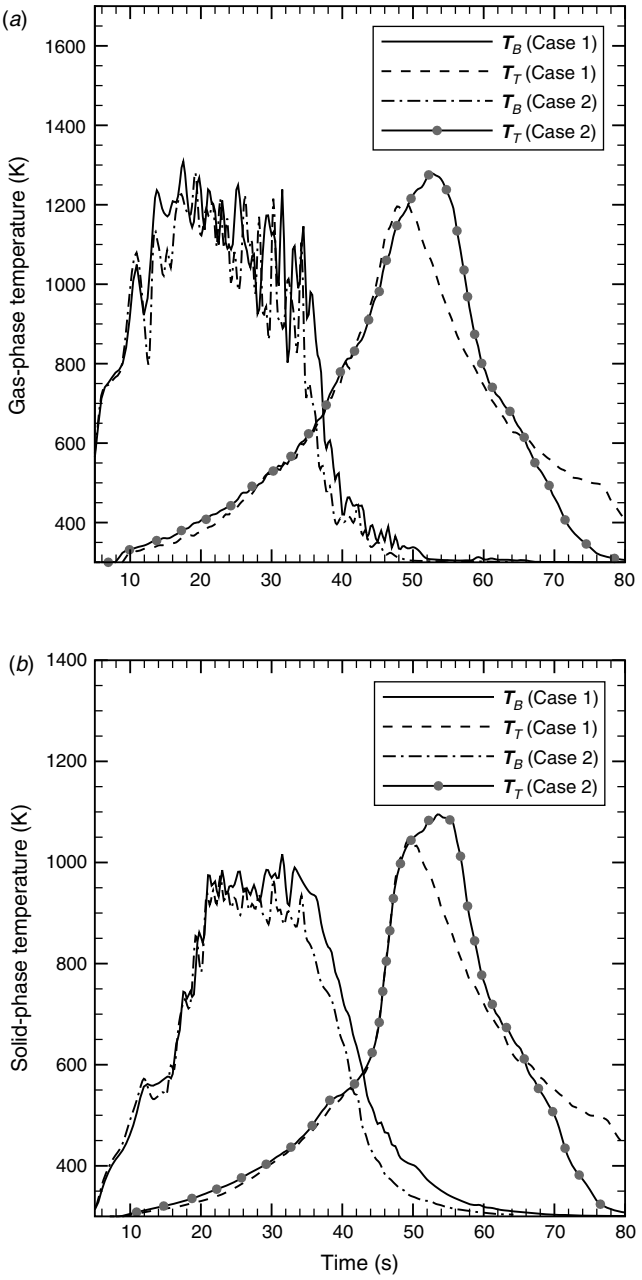

Fig. 5. Time evolution of (*a*) gas-phase temperature and (*b*) solid-phase temperature. T_T and T_B are obtained based on the averaging of temperatures on planes passing through the top and the bottom of the shrub; for crown fuel modelled with distributed bulk density (Case 1) and fixed bulk density (Case 2). Cases are from Table 1.

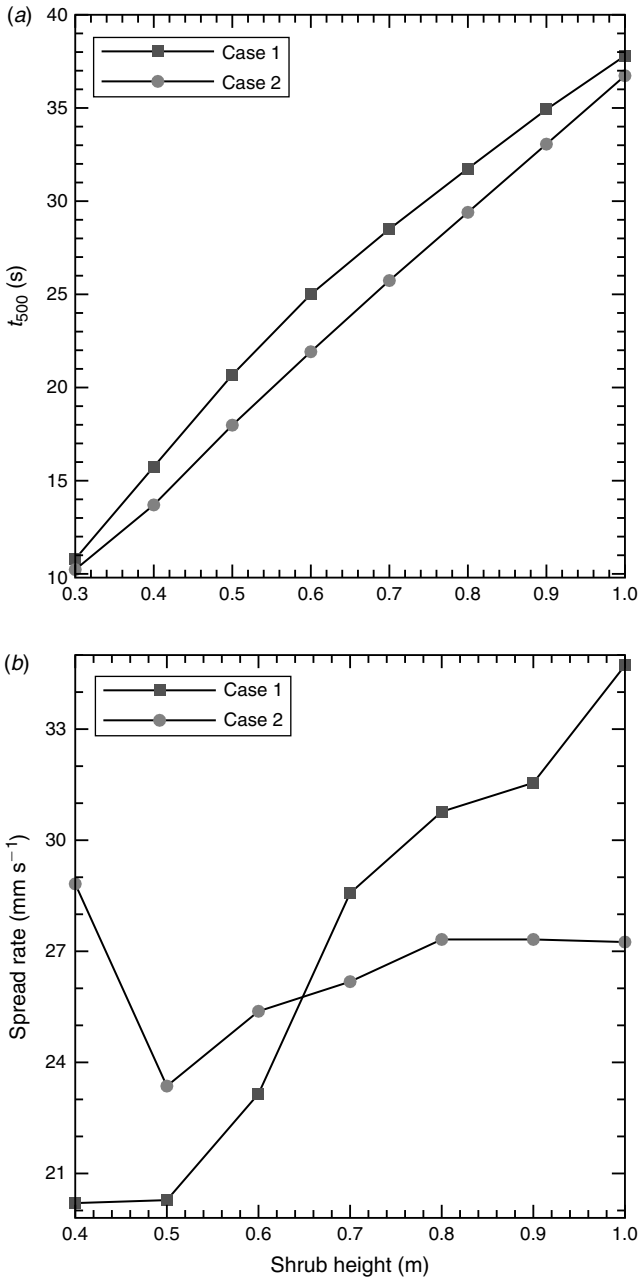

Fig. 6. (*a*) Spatial variation of t_{500} (time required by the horizontal shrub surface to reach an average temperature of 500 K); (*b*) spread rate *v.* shrub height (local spread rate at a generic location y_2 is calculated as $(y_2 - y_1)/(t_{500,2} - t_{500,1})$, therefore the x-axis starts from $y = 0.4$); for crown fuel modelled with distributed bulk density (Case 1) and fixed bulk density (Case 2). Cases are from Table 1.

Eqn 29, of the solid fuel particles located at the crown fuel bottom ($x = 0.8$, $y = 0.4$, $z = 0.8$ m) as a function of time for Case 1 and Case 2. It can be seen that the amount of energy supplied to the fuel particles remains the same for both cases as this location is near the ignition zone. In Case 1 this energy is distributed among a larger number of solid particles than in Case 2; thus, the crown fuel ignition is seen to occur earlier in time for Case 2. Moreover, a higher value of bulk density means more fuel is present in this region, for Case 1, resulting in a higher heat release. Therefore, once enough fuel starts to burn in this region, the spread rate increases dramatically for DBD in the range of $y = 0.5$–0.8 m as seen from Fig. 6*b*. In the upper half of the crown, bulk density for FBD is higher than that for DBD and hence the spread rate values for FBD in this region are observed to be lower than for DBD.

Based on the results presented in this section it can be conclusively stated that fire spread rate through a single shrub depends strongly on the distribution of bulk density.

Effect of fuel moisture content

In the models used in this study, the effect of fuel moisture on the ignition of the solid fuel is accounted for by the term $\bar{q}_{\text{mass}}$ appearing in the solid fuel energy balance Eqn 29.

In total, 10 simulations have been performed to investigate the effects of fuel moisture content on fire behaviour. Cases 3a to 3e include a crown fuel with a distributed bulk density, where the distribution is modelled as given by Eqn 52 and shown in Fig. 1*c*, with respective moisture contents of 20, 40, 60, 80 and 100%. Moisture content for Cases 4a to 4e varies in a similar manner as described above for Cases 3a to 3e, with the only difference that the crown fuel is modelled with a fixed bulk density of 3.8 kg m^{-3}, matching the average value of the polynomial distribution. The initial dry mass of the crown fuel, simulation setup, boundary conditions and initial flow field conditions for all 10 moisture cases are kept the same as discussed for Case 1.

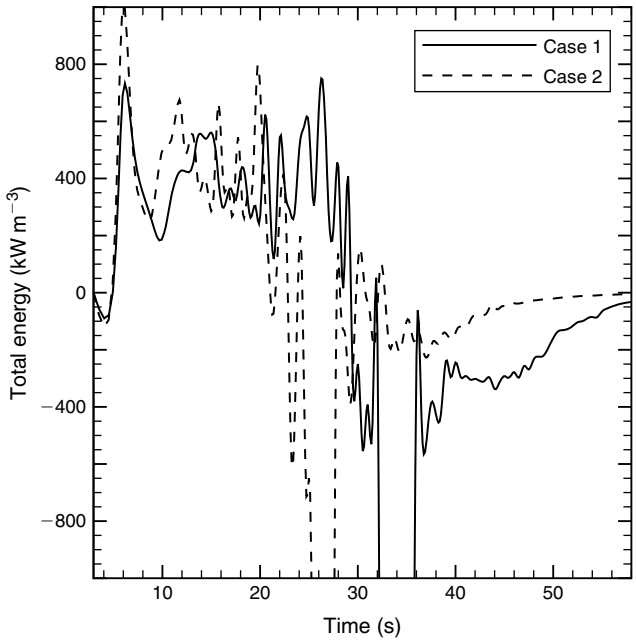

Fig. 7. Time evolution of total energy ($\boldsymbol{q}_{\text{conv}} + \boldsymbol{q}_{\text{rad}} + \boldsymbol{q}_{\text{mass}}$) of solid fuel particles located at $\boldsymbol{x} = 0.8$ m, $\boldsymbol{y} = 0.4$ m, $\boldsymbol{z} = 0.8$ m, a point near the bottom surface of the crown fuel, for distributed (Case 1) and fixed bulk density (Case 2) crown fuel models. Cases are from Table 1.

Here, first we discuss the results obtained from the simulations of Cases 4a to 4e and then include the results of Cases 3a to 3e. Fig. 8 shows the contour plots at various instances in time for a moisture content of 20% in the crown fuel (Case 4a). The snapshots show the gas-phase temperature (colour contours) and the bulk density (line contours) on an $\boldsymbol{x}$–$\boldsymbol{y}$ plane located at $\boldsymbol{z} = 0.8$ m. Similar contour plots are shown in Fig. 9, for a moisture content of 100% in crown fuel (Case 4e). Because the surface fuel model, crown fuel bulk density and amount of external energy supplied for ignition is the same for both cases, similar flow field patterns are generated at early times (before 10 s) for both cases.

For the case with lower moisture content, i.e. Case 4a, the crown fire initiates earlier in time (~9 s) as compared with Case 4e (~17 s), because the amount of heat required to evaporate the moisture and start the pyrolysis process is relatively low. From the snapshot at time 25 s in Fig. 8, it can be seen that a considerable portion of the crown fuel has started to burn for Case 4a, whereas for Case 4e, displayed in Fig. 9 for time 25 s, burning has been initiated only in a small portion of the fuel at crown bottom. This behaviour indicates that the ignition process is affected due to higher moisture content which in turn affects the fire spread rate. From the snapshot at 45 s in Fig. 8, it is seen that almost all the crown fuel is burnt out for Case 4a and therefore the fire starts to extinguish due to unavailability of fuel. On the other hand, in the snapshot at 45 s in Fig. 9, it is seen that although a considerable amount of the solid fuel is available, the fire intensity still reduces. The reason for this could be

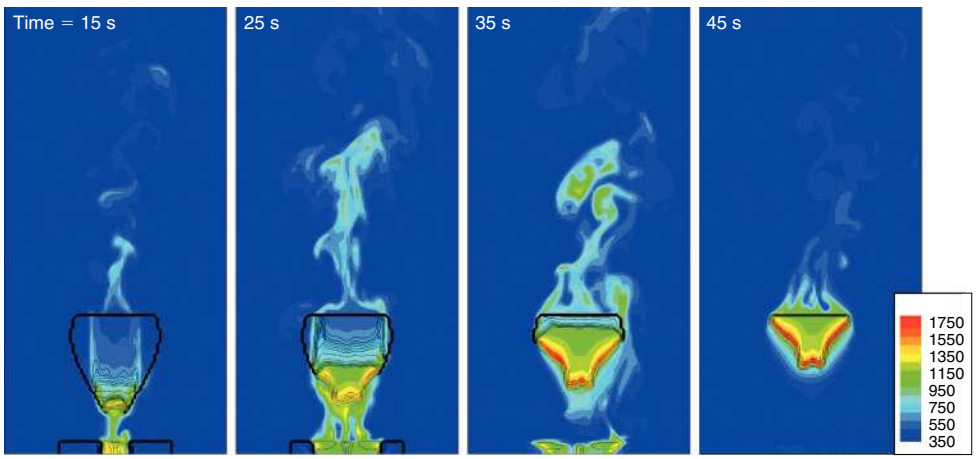

Fig. 8. Gas-phase temperature (K) (colour contours) with solid fuel bulk density (line contours) at various times for burning of crown fuel with moisture content of 20% (Case 4a, see Table 1). Snapshots are from a $\boldsymbol{xy}$-slice passing through $\boldsymbol{z} = 0.8$ m.

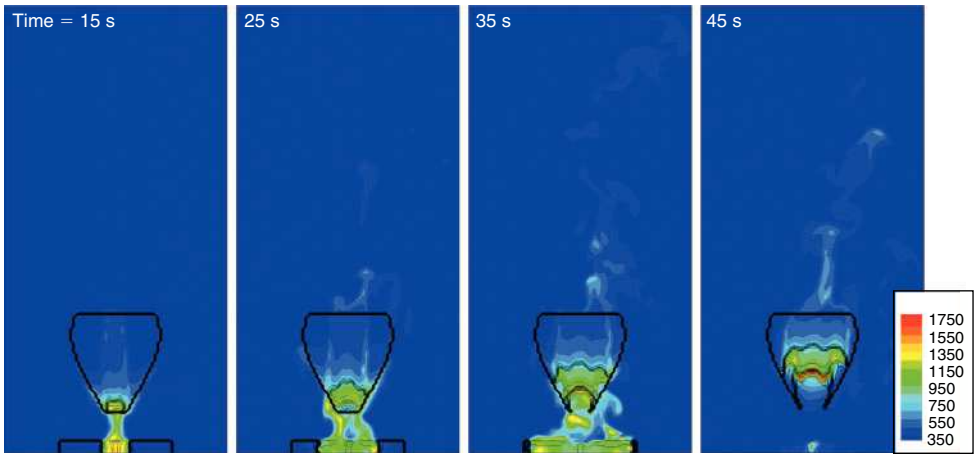

Fig. 9. Gas-phase temperature (K) (colour contours) with solid fuel bulk density (line contours) at various times for burning of crown fuel with moisture content of 100% (Case 4e, see Table 1). Snapshots are from a ***xy***-slice passing through $z = 0.8$ m.

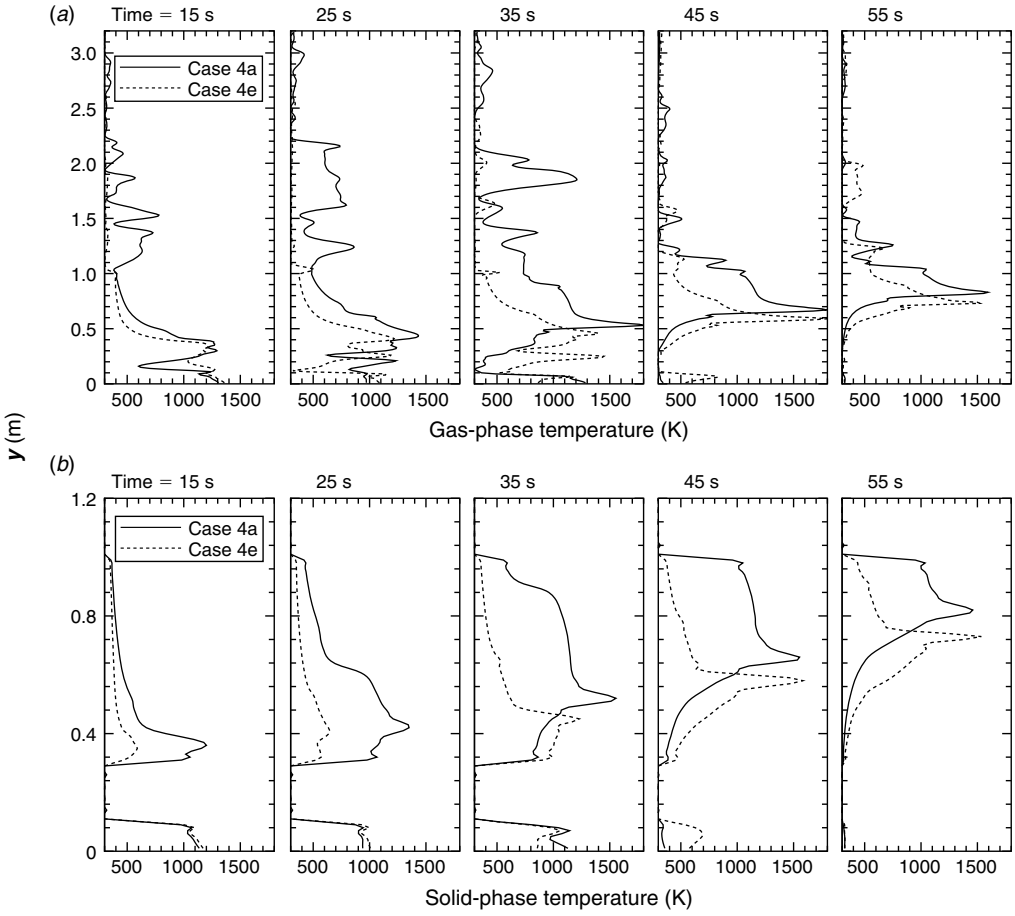

Fig. 10. Spatial variation of (*a*) gas-phase temperature, and (*b*) solid-phase temperature along a line passing through the domain centre, viz., $x = 0.8$ m, $z = 0.8$ m, in a ***y*** direction, for moisture contents of 20% (Case 4a) and 100% (Case 4e). Cases are from Table 1.

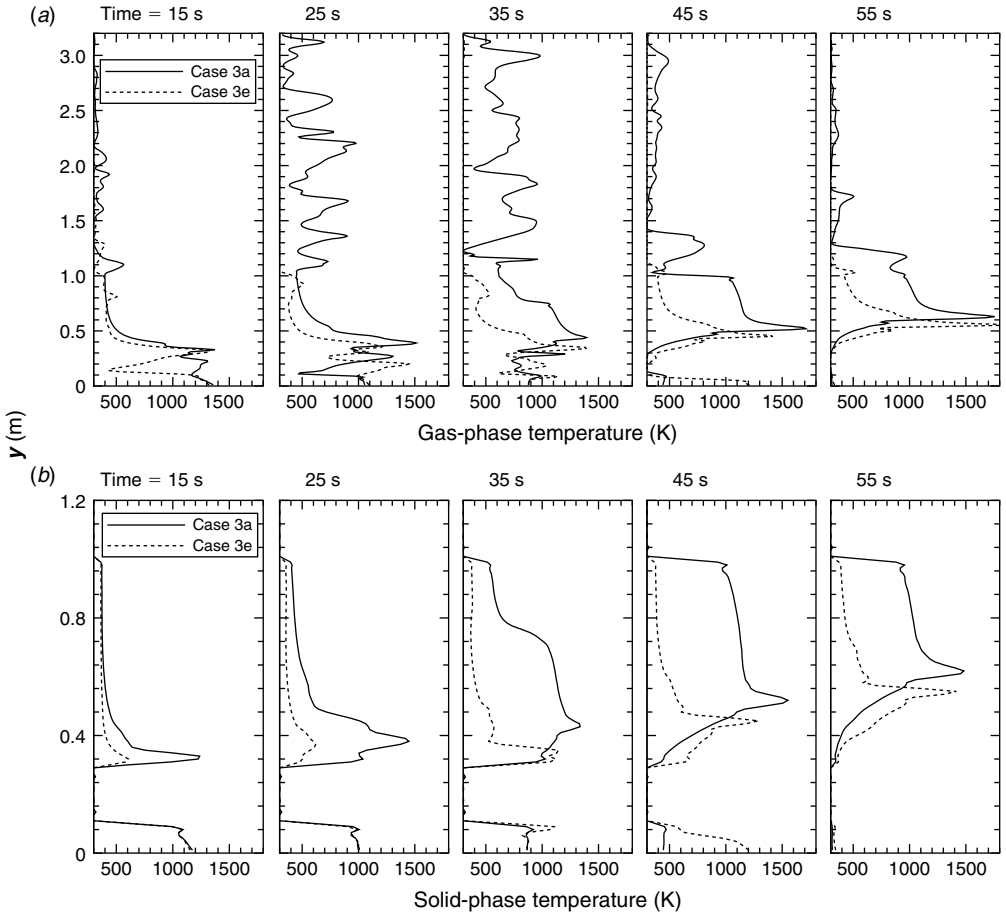

Fig. 11. Spatial variation of (*a*) gas-phase temperature, and (*b*) solid-phase temperature along a line passing through the domain centre, viz., $x = 0.8$ m, $z = 0.8$ m, in y direction, for moisture contents of 20% (Case 3a) and 100% (Case 3e). Cases are from Table 1.

that the amount of heat generated by flames is insufficient to heat unburnt fuel ahead of the flames, resulting in an imbalance between the amount of heat generated by the burning of fuel and the amount of heat required by the neighbouring unburnt fuel particles to ignite. Thus fire extinction for the high moisture content case (Case 4e) is not due to the unavailability of fuel.

To further investigate the effect of moisture content on distribution of gas- and solid-phase temperatures through the domain, instantaneous, local values of these variables are compared quantitatively. Fig. 10*a* shows the gas phase temperature for Case 4a and Case 4e at various time instances, along the y-axis passing through the centre of the domain ($x = 0.8$, $z = 0.8$ m). Similarly, Fig. 10*b* shows the plots of solid-phase temperature along the same probe line. From the plots at time 15, 25 and 35 s in Fig. 10 it is seen that both gas- and solid-phase temperatures for Case 4a are higher than respective gas- and solid-phase temperatures for Case 4e, indicating that intensity of fire is reduced by higher moisture content. In Fig. 10*b*, at times after 35 s, the solid-phase temperature is very high throughout the entire height of shrub for Case 4a, whereas in Case 4e, higher solid-phase temperatures are encountered in only a small portion of shrubs. This indicates that the time required for fire to consume the solid fuel increases with the rise in fuel moisture content. These observations, for cases where crown fuel is modelled with fixed bulk density, also apply to the simulations where the crown fuel is modelled with a distributed bulk density, which can be seen in Fig. 11. Fig. 11*a* shows gas-phase temperatures along a y-axis passing through the domain centre, for Case 3a and Case 3e, at various instances in time. Similarly, Fig. 11*b* shows solid-phase temperatures along the same probe line for Case 3a and 3e.

Fig. 12*a* shows the time evolution of crown fuel dry mass obtained from simulation of Cases 4a, 4b, 4c, 4d and 4e. This figure shows that the rate at which fire consumes the fuel decreases with an increase in moisture content. It can also be seen that the amount of fuel left unburnt when fire extinction in crown fuel occurs, increases with increasing fuel moisture content. Similar observations are made from Fig. 12*b*, which shows time history of crown fuel dry mass for Cases 3a, 3b, 3c, 3d and 3e.

Fig. 13*a* plots vertical fire spread rate through crown fuel as a function of fuel moisture content. Results obtained from all 10 moisture cases are shown in Fig. 13*a* along with the two experimental spread rate values obtained by Li (2011). The

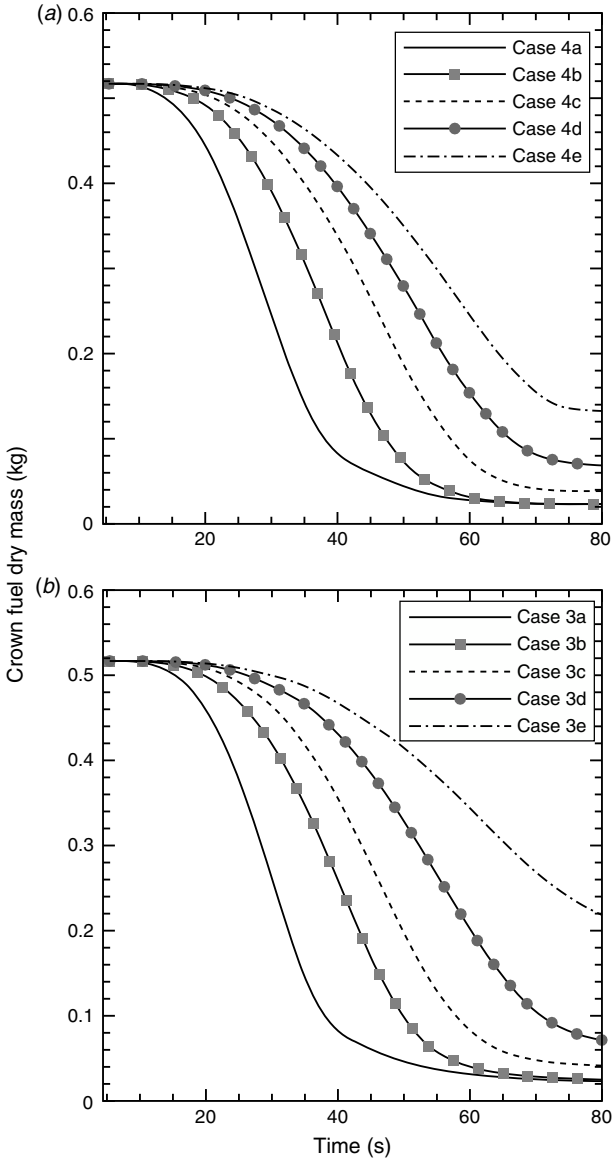

Fig. 12. Time evolution of crown fuel dry mass for (*a*) fixed bulk density (Cases 4a–e) and (*b*) distributed bulk density (Cases 3a–e). Cases are from Table 1.

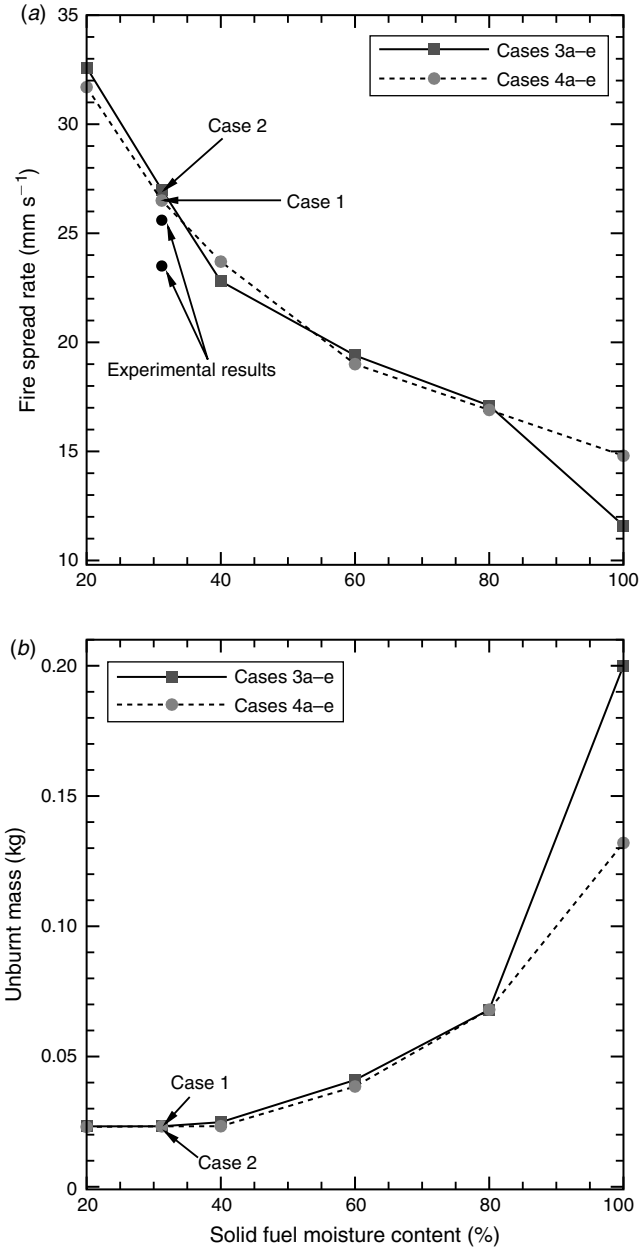

Fig. 13. (*a*) Average vertical fire spread rate and (*b*) unburnt mass as a function of fuel moisture content. Experimental data points in (*a*) are for two experimental tests (Li 2011) with the same moisture content of 31.2%. Cases are from Table 1.

vertical rate of spread for all cases is calculated using Eqn 53. It is seen that the fire spread rate decreases continuously as the moisture content increases from 20 to 100%, for both types of crown fuel models, i.e. crown fuel modelled with a FBD and with a DBD. A sharp decrease in spread rate is seen when moisture content increases from 20 to 40%. From moisture content 60 to 100%, the rate at which the fire spread rate decreases is almost steady, for cases using a FBD crown fuel model (Cases 4a to 4e). For fuel moisture content below 80%, vertical spread rates obtained from cases with a crown fuel model consisting of DBD (Cases 3a to 3d), are almost equivalent to those obtained from FBD cases (Cases 4a to 4d) with similar moisture contents, as seen from Fig. 13*a*.

Finally, shown in Fig. 13*b* is the mass of unburnt fuel plotted against the initial fuel moisture content for all 10 moisture cases. It can be seen that with the increase in moisture content, more of the crown fuel mass is left unburnt. The unburnt fuel mass increases dramatically within the range of moisture content between 80 and 100%, indicating that the fire spread in shrubs with higher moisture contents is slow or almost impossible. A similar observation was made for cases in which crown fuel was modelled with DBD, i.e. Cases 3a to 3e. For Case 3e as compared with Case 4e, fire spread rate decreases (Fig. 13*a*)

and unburnt mass increases (Fig. 13*b*) drastically indicating that higher resistance is offered to fire propagation when crown fuel is modelled with spatially distributed bulk density, having functional form given by Eqn 52. However, this observation is concerned with the spatial distribution of the bulk density rather than the moisture content effect.

Summary and conclusions

A previously developed physics-based model to simulate fire propagation through a porous solid fuel matrix, is described in detail. The model developed is not intended for field-scale simulations, but could help build better models adapted to field scales. The basic configuration studied involves a 0.1-m-deep surface fuel bed, and elevated, crown-like fuel matrix (chamise shrub) situated 0.2 m above the surface fuel. Global characteristics of fire behaviour predicted by the model are in fairly good agreement with available experimental results, except for the maximum mass loss rate value, which is overestimated by a factor of 1.4. Because we currently have limited access to the experimental facilities, extensive validation of the model through conducting more experiments currently is not feasible. More rigorous validation of the model through experimentation will be the focus of future work.

From the computational studies performed, it was observed that the spatial variation of crown fuel bulk density and the fuel moisture content have a significant effect on burning of isolated shrubs in still air. Both the crown fire initiation time and local vertical fire spread rate were influenced by variations in local fuel bulk density and overall fuel moisture content. The variation in bulk density in the vertical direction was modelled via a cubic polynomial with no variation assumed in horizontal planes. This bulk density distribution model resulted in an increase in the time required to initiate the combustion process within the shrub. A similar effect is seen when solid fuel contains higher amounts of moisture, though the mechanism causing the delay in ignition was found to be completely different. When a region has higher bulk density the heat received is distributed among a higher number of solid particles thus reducing the amount of heat gained by individual fuel particles which in turn delays the combustion process. On the other hand, fuel particles containing a higher moisture fraction delay the ignition as the drying process takes a significant amount of time to complete after which pyrolysis and char oxidation begins. Fire spreads in a distributed bulk density crown fuel (distribution modelled using a cubic polynomial), from one vertical location to another at uneven speeds; for example in the lower region fire propagation speed remains lower and then increases as it moves into the upper portion of the crown, when compared with spread rates in equivalent fixed bulk density crown. The time required to complete the burning of a shrub is thus not significantly affected when bulk density is distributed, but when moisture content is high, it increases considerably. A twofold increase in moisture content from 40 to 80% for instance results in a 63% increase in time required for complete burning of the shrub. It is also found that flames begin to extinguish at higher moisture contents even though a considerable amount of unburnt solid fuel is present in the shrub. The cause of these phenomena was found to be that fuel particles undergoing combustion did not generate sufficient energy required to initiate ignition of neighbouring fuel particles resulting in an increase in the amount of unburnt mass.

Acknowledgements

The authors are grateful to the National Science Foundation (Grant number CBET 1049560) for providing financial support for the work presented in this paper. We are pleased to acknowledge the High Performance Computing (HPC) resources provided by the Alabama Supercomputer Center.

References

Anderson HE (1969) Heat transfer and fire spread. USDA Forest Service, Intermountain Forest and Range Experiment Station, Research Paper RP-INT-69. (Ogden, UT)

Atreya A (1998) Ignition of fires. *Philosophical Transactions-Royal Society of London A – Mathematical. Physical and Engineering Sciences* **356**, 2787–2813. doi:10.1098/RSTA.1998.0298

Babrauskas V (2008) Heat release rates. In 'The SFPE Handbook of Fire Protection Engineering', 4th edn. , pp. 3-1–3-59. (National Fire Protection Association: Quincy, MA)

Baum MM, Street PJ (1971) Predicting the combustion behaviour of coal particles. *Combustion Science and Technology* **3**(5), 231–243. doi:10.1080/00102207108952290

Bird GA (1994) 'Molecular Gas Dynamics and the Direct Simulation of Gas Flows', 2nd edn. (Oxford University Press: Oxford, MA)

Boudier G, Gicquel LYM, Poinsot TJ (2008) Effects of mesh resolution on large eddy simulation of reacting flows in complex geometry combustors. *Combustion and Flame* **155**, 196–214. doi:10.1016/J.COMBUSTFLAME.2008.04.013

Branley N, Jones WP (2001) Large eddy simulation of a turbulent non-premixed flame. *Combustion and Flame* **127**, 1914–1934. doi:10.1016/S0010-2180(01)00298-X

Butler BW (1993) Experimental measurements of radiant heat fluxes from simulated wildfire flames. In 'Proceedings of the 12th International Conference on Fire and Forest Meteorology', 26–28 October 1993, Jekyll Island, GA. pp. 104–112. (Society of American Foresters: Madison, WI)

Chandrasekhar S (1960) 'Radiative Transfer.' (Dover: New York)

Clift R, Grace JR, Weber ME (1978) 'Bubbles, Drops, and Particles.' (Academic Press: New York)

Countryman CM, Philpot CW (1970) Physical characteristics of chamise as a wildland fuel. USDA Forest Service, Pacific Southwest Forest & Range Experiment Station, Research Paper PSW-RP-66. (Berkeley, CA)

Dimitrakopoulos AP, Papaioannou KK (2001) Flammability assessment of Mediterranean forest fuels. *Fire Technology* **37**, 143–152. doi:10.1023/A:1011641601076

Dong Y-H, Chen L-F (2011) The effect of stable stratification and thermophoresis on fine particle deposition in a bounded turbulent flow. *International Journal of Heat and Mass Transfer* **54**, 1168–1178. doi:10.1016/J.IJHEATMASSTRANSFER.2010.11.005

Erlebacher G, Hussaini MY, Speziale CG, Zang TA (1992) Toward the large-eddy simulation of compressible turbulent flows. *Journal of Fluid Mechanics* **238**, 155–185. doi:10.1017/S0022112092001678

Germano M, Piomelli U, Moin P, Cabot WH (1991) A dynamic subgrid-scale eddy viscosity model. *Physics of Fluids* **3**, 1760–1765. doi:10.1063/1.857955

Ghosal S, Lund TS, Moin P, Akselvoll K (1995) A dynamic localization model for large-eddy simulation of turbulent flows. *Journal of Fluid Mechanics* **286**, 229–255. doi:10.1017/S0022112095000711

Grishin AM (1997) 'Mathematical Modelling of Forest Fires and New Methods of Fighting Them.' (Ed. FA Albini) (Publishing House of Tomsk State University: Tomsk, Russia)

Grosshandler WL (1993) RADCAL: a narrow-band model for radiation calculations in a combustion environment. National Institute of Standards and Technology, Technical Note 1402. (Gaithersburg, MD)

Gullbrand J, Chow FK (2003) The effect of numerical errors and turbulence models in large-eddy simulations of channel flow, with and without explicit filtering. *Journal of Fluid Mechanics* **495**, 323–341. doi:10.1017/S0022112003006268

Janicka J, Sadiki A (2005) Large eddy simulation of turbulent combustion systems. *Proceedings of the Combustion Institute* **30**, 537–547. doi:10.1016/J.PROCI.2004.08.279

Kaplan C, Shaddix CR, Smyth KC (1996) Computations of enhanced soot production in time-varying CH_4/air diffusion flames. *Combustion and Flame* **106**, 392–405. doi:10.1016/0010-2180(95)00258-8

Kee RJ, Rupley FM, Miller JA (1989) CHEMKIN-II: a Fortran chemical kinetics package for the analysis of gas-phase chemical kinetics. Sandia National Laboratories, report number SAND89–8009B. (Livermore, CA)

Kee RJ, Rupley FM, Miller JA (1990) The Chemkin thermodynamic data base. Sandia National Laboratories, report number SAND-87-8215B. (Livermore, CA)

Kim J, Moin P (1985) Application of a fractional-step method to incompressible Navier–Stokes equations. *Journal of Computational Physics* **59**, 308–323. doi:10.1016/0021-9991(85)90148-2

Larini M, Giroud F, Porterie B, Loraud JC (1998) A multiphase formulation for fire propagation in heterogeneous combustible media. *International Journal of Heat and Mass Transfer* **41**, 881–897. doi:10.1016/S0017-9310(97)00173-7

Lathrop KD, Carlson BG (1965) Discrete ordinates angular quadrature of neutron transport equation. Los Alamos Scientific Laboratory, Technical Information Series Report LASL-3186 (Los Alamos, NM)

Leonard BP (1979) A stable and accurate convective modelling procedure based on quadratic upstream interpolation. *Computer Methods in Applied Mechanics and Engineering* **19**, 59–98. doi:10.1016/0045-7825(79)90034-3

Li J (2011) Experimental investigation of bulk density and its role in fire behavior in live shrub fuels. MSc thesis, University of California–Riverside, Riverside, CA.

Lilly DK (1991) A proposed modification of the Germano subgrid scale closure method. *Physics of Fluids* **4**, 633–635.

Mahesh K, Constantinescu G, Apte S, Iaccarino G, Ham F, Moin P (2006) Large-eddy simulation of reacting turbulent flows in complex geometries. *Journal of Applied Mechanics* **73**, 374–381. doi:10.1115/1.2179098

Manzello SL, Maranghides A, Mell WE (2007) Firebrand generation from burning vegetation. *International Journal of Wildland Fire* **16**, 458–462. doi:10.1071/WF06079

Mehta RS, Haworth DC, Modest MF (2010) Composition PDF/photon Monte Carlo modeling of moderately sooting turbulent jet flames. *Combustion and Flame* **157**, 982–994. doi:10.1016/J.COMBUSTFLAME.2009.11.009

Mell W, Jenkins MA, Gould J, Cheney P (2007) A physics-based approach to modelling grassland fires. *International Journal of Wildland Fire* **16**, 1–22. doi:10.1071/WF06002

Mell W, Maranghides A, McDermott R, Manzello SL (2009) Numerical simulation and experiments of burning douglas fir trees. *Combustion and Flame* **156**, 2023–2041. doi:10.1016/J.COMBUSTFLAME.2009.06.015

Modest MF (2003) 'Radiative Heat Transfer', 2nd edn. (Academic Press: New York)

Morvan D (2011) Physical phenomena and length scales governing the behaviour of wildfires: a case for physical modelling. *Fire Technology* **47**, 437–460. doi:10.1007/S10694-010-0160-2

Morvan D, Dupuy JL (2001) Modeling of fire spread through a forest fuel bed using a multiphase formulation. *Combustion and Flame* **127**, 1981–1994. doi:10.1016/S0010-2180(01)00302-9

Nagle J, Strickland-Constable RF (1962) Oxidation of carbon between 1000–2000°C. In 'Proceedings of the Fifth Conference on Carbon', 19–23 June 1961, University Park, PA. Vol. 1, pp. 154–164. (Pergamon Press: New York)

Pereira JCF, Sousa JMM (1993) Finite volume calculations of self-sustained oscillations in a grooved channel. *Journal of Computational Physics* **106**, 19–29. doi:10.1006/JCPH.1993.1087

Pickford SG, Fahnestock GR, Ottmar R (1980) Weather, fuel, and lightning fires in Olympic National Park. *Northwest Science* **54**, 92–105.

Porterie B, Morvan D, Loraud JC, Larini M (2000) Firespread through fuel beds: modelling of wind aided fires and included hydrodynamics. *Physics of Fluids* **12**, 1762–1782. doi:10.1063/1.870426

Ragland KW, Aerts DJ, Baker AJ (1991) Properties of wood for combustion analysis. *Bioresource Technology* **37**, 161–168. doi:10.1016/0960-8524(91)90205-X

Rehm RG, Baum HP (1978) The equations of motion for thermally driven, buoyant flows. *Journal of Research of the National Bureau of Standards* **83**, 297–308. doi:10.6028/JRES.083.019

Renkin RA, Despain DG (1992) Fuel moisture, forest type, and lightning-caused fire in Yellowstone National Park. *Canadian Journal of Forest Research* **22**, 37–45. doi:10.1139/X92-005

Rothermel RC (1972) A mathematical model for predicting fire spread in wildland fuels. USDA Forest Service, Intermountain Forest and Range Experiment Station, General Technical Report INT-115. (Ogden, UT)

Speziale CG, Erlebacher G, Zang TA, Hussaini MY (1988) The subgrid-scale modeling of compressible turbulence. *Physics of Fluids* **31**, 940–942. doi:10.1063/1.866778

Sullivan AL (2009) Wildland surface fire spread modeling, 1990–2007. 1. Physical and quasi-physical models. *International Journal of Wildland Fire* **18**, 349–368. doi:10.1071/WF06143

Tachajapong W (2008) Understanding crown fire initiation via experimental and computational modeling. PhD Thesis, University of California–Riverside, Riverside, CA.

VanWagner CE (1977) Conditions for the start and spread of crown fire. *Canadian Journal of Forest Research* **7**, 23–34. doi:10.1139/X77-004

Wang L, Haworth DC, Turns SR, Modest MF (2005) Interactions among soot, thermal radiation, and NO_x emissions in oxygen-enriched turbulent nonpremixed flames: a computational fluid dynamics modeling study. *Combustion and Flame* **141**, 170–179. doi:10.1016/J.COMBUSTFLAME.2004.12.015

Yoshizawa A (1986) Statistical theory for compressible turbulent shear flows, with the application to subgrid modeling. *Physics of Fluids* **29**, 2152–2164. doi:10.1063/1.865552

Zhou X, Mahalingam S (2002) A flame surface density based model for large eddy simulation of turbulent nonpremixed combustion. *Physics of Fluids* **14**, 77–80. doi:10.1063/1.1518691

Zhou X, Mahalingam S (2003) A suitable mixture fraction for diffusion flames of wood pyrolysis gas. *Combustion and Flame* **133**, 197–199. doi:10.1016/S0010-2180(02)00550-3

Zhou X, Pakdee W, Mahalingam S (2004) Assessment of a flame surface density-based subgrid turbulent combustion model for nonpremixed flames of wood pyrolysis gas. *Physics of Fluids* **16**, 3795–3807. doi:10.1063/1.1778371

Zhou X, Mahalingam S, Weise D (2005) Modeling of marginal burning state of fire spread in live chaparral shrub fuel bed. *Combustion and Flame* **143**, 183–198. doi:10.1016/J.COMBUSTFLAME.2005.05.013

Zhou X, Mahalingam S, Weise D (2007) Experimental study and large eddy simulation of effect of terrain slope on marginal burning in shrub fuel beds. *Proceedings of the Combustion Institute* **31**, 2547–2555. doi:10.1016/J.PROCI.2006.07.222